Geophysical Research Letters

RESEARCH LETTER
10.1029/2026GL122823

The Lifecycle of Tracer Variance in the North Atlantic

Espe Broullón[1], Richard G. Williams[2], Alberto C. Naveira Garabato[1], Louis Clément[3], and Bieito Fernández Castro[1]

[1]Ocean and Earth Science, University of Southampton, Southampton, UK, [2]Earth, Ocean and Ecological Sciences, School of Environmental Sciences, University of Liverpool, Liverpool, UK, [3]National Oceanography Centre, Southampton, UK

Key Points:

- Tracer variance is produced and transferred downscale by turbulent stirring, transported by currents, and dissipated by molecular diffusion
- Diapycnal variance transfer by microscale turbulence dominates in quiescent regions, such as the centre of subtropical gyres
- Isopycnal variance transfer by mesoscale eddies and transport by currents dominates in dynamic regions, such as the gyre flanks

Supporting Information:

Supporting Information may be found in the online version of this article.

Correspondence to:

E. Broullón,
E.Broullon-Mandado@soton.ac.uk

Citation:

Broullón, E., Williams, R. G., Naveira Garabato, A. C., Clément, L., & Fernández Castro, B. (2026). The lifecycle of tracer variance in the North Atlantic. *Geophysical Research Letters*, *53*, e2026GL122823. https://doi.org/10.1029/2026GL122823

Received 5 MAR 2026
Accepted 11 MAY 2026

Abstract Oceanic tracer distributions are shaped by turbulent mixing, which may be understood via a traver variance budget. There is a tracer variance lifecycle: variance production by turbulent flows stirring large-scale gradients, redistribution by currents, and variance dissipation by molecular diffusion. A comprehensive tracer variance budget, including variance transport, is diagnosed from North Atlantic hydrographic observations and reveals three different regimes. In the subtropical thermocline, there is a local balance between diapycnal production by microscale turbulence and molecular dissipation. In intermediate waters and the subpolar gyre, the local balance is between isopycnal production by mesoscale stirring and dissipation. Near gyre boundaries, a three-way balance emerges between isopycnal production by mesoscale stirring, variance transport by currents, and dissipation downstream. Transitions between mixing regimes are determined by water-mass contrasts and circulation strength. Our expectation is that these different mixing regimes apply to the global ocean and affect how the ocean sequesters and redistributes anthropogenic heat.

Plain Language Summary Horizontal and vertical temperature contrasts in the ocean are mixed away due to the stirring effect of kilometre-scale swirls and centimetre-scale turbulence. This mixing affects the ocean storage of heat, modifying how heat is transferred from the surface into the ocean interior. Mixing is quantified here over the North Atlantic Ocean by applying a new methodology to thousands of observations from profiling floats. In the centre of the subtropical gyre, heat is mixed vertically by centimetre-scale turbulence. Over the flanks of the subtropical gyre and in the subpolar region, heat is instead stirred horizontally by kilometre-scale eddies, creating warm and cold filaments. In regions of strong flows, these warm and cold filaments are carried by ocean currents for hundreds of kilometres before they blend into surrounding waters, resulting in mixing far away from the location where stirring happens. These mixing and stirring processes ultimately then affect how the global ocean sequesters anthropogenic heat in a warming climate.

1. Introduction

Air-sea interactions form temperature-salinity contrasts in the mixed layer that spread into the ocean interior and are modified by mixing. This interplay of surface forcing and interior mixing controls the ocean storage of heat and freshwater, and so affects the global thermohaline circulation (Döös et al., 2012; Fernández Castro et al., 2026; Groeskamp et al., 2019; Hieronymus et al., 2014; Zika et al., 2012).

Mixing of tracers, including heat and freshwater, is the result of turbulent stirring and molecular diffusion (Garrett, 1983; Joyce, 1977; Ledwell et al., 1998; Sundermeyer & Price, 1998). The mixing process may be understood in terms of a lifecycle of tracer variance (given by the square of turbulent fluctuations in the tracer; Osborn & Cox, 1972). Tracer variance is produced through turbulent stirring acting on large-scale tracer gradients, transferred downscale through further stirring by progressively smaller flows, and eventually dissipated by molecular diffusion (Garrett, 1983; Naveira Garabato et al., 2016; Smith & Ferrari, 2009). The downscale transfer of variance occurs primarily via two routes, leading to two distinct mixing regimes: anisotropic mesoscale stirring acting along neutral density surfaces and isotropic microscale turbulence drawing variance from tracer gradients across density surfaces, referred to as isopycnal stirring and diapycnal mixing respectively (Ferrari & Polzin, 2005; Fernández Castro et al., 2024; Naveira Garabato et al., 2011).

The rates of downscale transfer and dissipation of tracer variance are usually assumed to balance each other locally (Osborn & Cox, 1972). This assumption underpins parameterization of turbulent mixing processes in climate-scale ocean models (Cherian et al., 2024), and the quantification of mixing rates from microscale observations (Davis, 1994; Ledwell et al., 1998).

A problem with this assumption of a local balance is that tracer variance can take time to cascade to dissipative scales, particularly density-compensated filamentary structures produced via mesoscale stirring (Naveira Garabato et al., 2016). Tracer variance can be redistributed by the circulation, which may lead to sources and sinks of variance not locally balancing, as illustrated in eddy-resolving ocean model experiments for a dynamic tracer (Holland & Rhines, 1980; Marshall, 1984; Rhines & Holland, 1979). The lifecycle of tracer variance may be extended to include transport by the circulation, where tracer variance is formed, transported, and ultimately dissipated at molecular scales. If transport of tracer variance is important, stirring processes acting in one place end up changing the background tracer distribution in a different place some distance away, rather than locally.

Our study expands the theory for diagnosing the contributions of microscale and mesoscale turbulence to the mixing of heat and salt (Ferrari & Polzin, 2005; Naveira Garabato et al., 2016), by explicitly including transport of tracer variance (Section 2). This work builds upon our method to diagnose diapycnal and isopycnal stirring rates from Argo observations (Broullón et al., 2026b), which is validated by independent microstructure data in the eastern North Atlantic (Ferrari & Polzin, 2005). Our analysis is applied over the entire North Atlantic (Section 3), a climatically important basin that is strongly ventilated (Marshall et al., 1993; MacGilchrist et al., 2020) and plays a significant role in sequestering anthropogenic heat from the atmosphere (Li et al., 2023). The temperature variance lifecycle is assessed on neutral density surfaces spanning the thermocline and intermediate waters (Section 4; a salinity variance budget is presented in Supporting Information S1). We identify three different mixing regimes that are linked to the distribution of water masses and the circulation strength (Section 5). These different mixing regimes are expected to carry over to the rest of the global ocean and affect how anthropogenic heat and other tracers are redistributed.

2. Theory

2.1. Tracer Variance Budget Including Transport

A budget for tracer variance (Davis, 1994; Ferrari & Polzin, 2005; Garrett, 2001) involves a balance between tendency of variance, divergence of variance transport, production of variance from the projection of the eddy tracer flux onto the background tracer gradient, and dissipation of tracer variance by molecular diffusion:

$$\underbrace{\frac{\partial \overline{c'^2}}{\partial t}}_{\substack{\text{tendency}\\ \text{of variance}}} + \underbrace{\nabla \cdot \left(\overline{\mathbf{u}}\, \overline{c'^2} + \overline{\mathbf{u}' c'^2} - \kappa_c \nabla \overline{c'^2} \right)}_{\substack{\text{divergence of}\\ \text{variance transport}}} + \underbrace{2\overline{\mathbf{u}' c'} \cdot \nabla \overline{c}}_{\substack{\text{eddy production}\\ \text{of variance}}} = -\underbrace{2\kappa_c \overline{(\nabla c')^2}}_{\substack{\text{dissipation}\\ \text{of variance}}}, \tag{1}$$

where c is a generic tracer, $\mathbf{u}$ is the three-dimensional velocity, κ_c is the molecular diffusivity, and molecular dissipation of tracer variance is represented by $\chi_c \equiv 2\kappa_c \overline{(\nabla c')^2}$. A time mean is denoted by an overbar, representing an average over many eddy lifecycles, and a time deviation denoted by a prime (see Appendix A for derivation).

The tracer variance transport (second term in Equation 1) includes variance advection by the time-mean flow, $\overline{\mathbf{u}} \overline{c'^2}$, and by mesoscale eddies, $\overline{\mathbf{u}' c'^2}$, and molecular diffusive transfer of variance, $-\kappa_c \nabla \overline{c'^2}$. Here, we wish to include the effect of time-mean advection and neglect molecular diffusion as being relatively small (Davis, 1994). While eddy advection of tracer variance is potentially important based upon scaling (Davis, 1994), it is not possible to infer this term from our observations. Hence, we analyze the tracer variance budget (Equation 1) in a simplified, advective form (see Appendix A):

$$\frac{\partial \overline{c'^2}}{\partial t} + \overline{\mathbf{u}} \cdot \nabla \overline{c'^2} + 2\overline{\mathbf{u}' c'} \cdot \nabla \overline{c} = -\chi_c. \tag{2}$$

This tracer variance balance may be written in terms of the Lagrangian evolution of tracer variance, $D\overline{c'^2}/Dt$ following the time-mean flow, the eddy production of variance, $2\overline{\mathbf{u}' c'} . \nabla \overline{c}$, and the molecular dissipation of tracer variance,

$$\underbrace{-\frac{D\overline{c'^2}}{Dt}}_{\substack{\text{Lagrangian}\\ \text{evolution}}} - \underbrace{2\overline{\mathbf{u}'c'}\cdot\nabla\overline{c}}_{\substack{\text{eddy}\\ \text{production}}} = \underbrace{\chi_c}_{\substack{\text{molecular}\\ \text{dissipation}}}, \tag{3}$$

where $D/Dt \equiv \partial/\partial t + \overline{\mathbf{u}}.\nabla$ henceforth represents the Lagrangian rate of change following the time-mean flow.

There is a down-gradient eddy tracer flux if dissipation of tracer variance dominates in Equation 3, such that the sign of the scalar product of the eddy tracer flux and tracer gradient, $\overline{\mathbf{u}'c'}.\nabla\overline{c}$, is negative (Holland & Rhines, 1980; Marshall, 1984; Rhines & Holland, 1979). Conversely, the eddy tracer flux can either be down- or up-gradient if the Lagrangian evolution of tracer variance dominates in Equation 3: there is a down-gradient eddy tracer flux when the tracer variance increases downstream, $D\overline{c'^2}/Dt > 0$, and instead an up-gradient eddy tracer flux when both the tracer variance decreases downstream, $D\overline{c'^2}/Dt < 0$, and molecular dissipation is small (Williams et al., 2007; Wilson & Williams, 2006).

2.2. Applying a Triple Decomposition for the Eddy Tracer Flux

The projection of the eddy tracer flux onto the background tracer gradient, $-2\overline{\mathbf{u}'c'}.\nabla\overline{c}$, can be viewed as an eddy production of tracer variance (Davis, 1994; Osborn & Cox, 1972). This eddy production of variance is separated into mesoscale eddy and microscale components (Garrett, 2001), with the mesoscale eddy component directed along a neutral density surface and the microscale component directed across neutral density surfaces (Ferrari & Polzin, 2005; Naveira Garabato et al., 2016):

$$\overline{\mathbf{u}'c'}\cdot\nabla\overline{c} = \overline{\mathbf{u}'c'}|_e\cdot\nabla_{\|}\overline{c} + \overline{\mathbf{u}'c'}|_t\cdot\nabla_{\perp}\overline{c}, \tag{4}$$

where subscript e denotes mesoscale eddy contributions and subscript t indicates microscale turbulent contributions; $\nabla_{\|}$ is the gradient operator along a neutral density surface, and $\nabla_{\perp}$ is the gradient operator across a neutral density surface.

Combining the tracer variance Equation 3 with the eddy tracer flux decomposition (Equation 4),

$$-2\overline{\mathbf{u}'c'}|_e\cdot\nabla_{\|}\overline{c} - 2\overline{\mathbf{u}'c'}|_t\cdot\nabla_{\perp}\overline{c} = \chi_c + \frac{D\overline{c'^2}}{Dt}, \tag{5}$$

together with closures for the mesoscale eddy and microscale turbulent tracer fluxes,

$$\begin{aligned}\overline{\mathbf{u}'c'}|_e &= -K_{\|}\nabla_{\|}\overline{c},\\ \overline{\mathbf{u}'c'}|_t &= -K_{\perp}\nabla_{\perp}\overline{c},\end{aligned} \tag{6}$$

leads to a tracer variance budget connecting production, dissipation and advection of variance,

$$\underbrace{2K_{\|}\left(\nabla_{\|}\overline{c}\right)^2}_{\substack{\text{mesoscale}\\ \text{production}}} + \underbrace{2K_{\perp}\left(\nabla_{\perp}\overline{c}\right)^2}_{\substack{\text{microstructure}\\ \text{production}}} = \underbrace{\chi_c}_{\substack{\text{molecular}\\ \text{dissipation}}} + \underbrace{\frac{D\overline{c'^2}}{Dt}}_{\text{advection}}, \tag{7}$$

which can be written more concisely as

$$P_{\|} + P_{\perp} = \chi_c + \frac{D\overline{c'^2}}{Dt}, \tag{8}$$

where $K_{\parallel}$ is the mesoscale isopycnal diffusivity, $K_{\perp}$ is the microscale diapycnal diffusivity, $P_{\parallel} \equiv 2K_{\parallel}\left(\nabla_{\parallel}\overline{c}\right)^2$ is the isopycnal production by mesoscale stirring, and $P_{\perp} \equiv 2K_{\perp}(\nabla_{\perp}\overline{c})^2$ is the diapycnal production by microscale turbulence.

3. Methods

Our approach to analyze the temperature variance budget follows Broullón et al. (2026b), where the methods to diagnose mixing were validated against microstructure data (Ferrari & Polzin, 2005).

3.1. Argo Data Set

Temperature profiles were obtained from Argo floats over the North Atlantic (Argo, 2025; Wong et al., 2020), in a box ranging from 0°N to 65°N and from 80°W to 0°W, from year 2006 to 2025. To resolve finescale variability, the data is required to have a vertical resolution of at least 5 m throughout the upper 1,000 m, providing 119,777 profiles. Each profile is averaged onto a vertical grid with 2 m resolution and gaps included where there is missing data due to coarser vertical resolution.

For each profile, vertically smooth conservative temperature, $\widetilde{\Theta}$, is computed by fitting a second-order polynomial as a function of neutral density, γ^n (Jackett & McDougall, 1997), within a 400-dbar sliding window. Thermal variance for each profile was defined as the squared fluctuations relative to the smooth fields: $\Theta'^2 = (\Theta - \widetilde{\Theta})^2$. This estimate of thermal variance is, effectively, for the mesoscale variability, as the smoothed profiles isolate density-compensated fine-structures generated by mesoscale stirring (Fernández Castro et al., 2024). Microscale variance could only be quantified with direct microstructure observations, but is orders of magnitude smaller than mesoscale variance, and therefore is neglected.

3.2. Finescale Parameterization

Profiles of turbulent energy dissipation rates, ε, and diapycnal diffusivity, $K_{\perp}$, were obtained using strain-based fine-scale parameterizations (Kunze et al., 2006; Voet et al., 2023; Whalen et al., 2012). These variables were derived on 200 m thick segments overlapping by 50 m. Data shallower than either the mixed-layer or 150 m were excluded, where the mixed-layer depth was defined as the depth at which potential density exceeded the surface value by 0.03 kg m^{-3}.

Profiles of conservative temperature variance dissipation rates, χ_{Θ}, were diagnosed following Osborn and Cox (1972) and Joyce (1977),

$$\chi_{\Theta} = 2K_{\perp}(\nabla_{\perp}\Theta)^2 \approx 2K_{\perp}\left(\frac{\partial\Theta}{\partial z}\right)^2, \tag{9}$$

where the vertical temperature gradient, $\partial\Theta/\partial z$, includes structures associated with mesoscale stirring and the background temperature gradient, and is evaluated at 2 m resolution.

The microscale, diapycnal production of thermal variance was estimated using smoothed tracer profiles in (Equation 9), which exclude mesoscale fluctuations (Fernández Castro et al., 2024):

$$P_{\perp,\Theta} = 2K_{\perp}\left(\nabla_{\perp}\widetilde{\Theta}\right)^2 \approx 2K_{\perp}\left(\frac{\partial\widetilde{\Theta}}{\partial z}\right)^2, \tag{10}$$

where the smoothed gradients, $\nabla_{\perp}\widetilde{\Theta}$, were calculated at 2 m resolution.

3.3. Tracer Variance Budget

The tracer variance budget for conservative temperature was evaluated using a time and space mean for 1° latitude-longitude boxes (Figure S1 in Supporting Information S1). Within each box, outliers in mixing diagnostics were removed by excluding ε values exceeding three standard deviations. Time-mean profiles of mixing rates and property-related quantities (Θ, Θ'^2, $\frac{\partial\Theta}{\partial z}$ and $\frac{\partial S}{\partial z}$) were calculated in a neutral density grid ranging

from 24.75 to 28.05 kg m^{-3} with grid spacing of 0.05 kg m^{-3}. The sensitivity of our diagnostics to horizontal resolution was assessed by performing alternative calculations in 3° boxes (Figures S5–S7 and S9 in Supporting Information S1).

The temperature variance budget in (Equation 8) uses the binned estimates of tracer variance dissipation (Equation 9) and diapycnal production (Equation 10) derived from individual profiles. The Lagrangian advection in (Equation 8), $\frac{D\overline{\Theta'^2}}{Dt}$, was estimated assuming a steady state and with advection of tracer variance from the time-mean geostrophic flow,

$$\frac{D\overline{\Theta'^2}}{Dt} \sim \overline{\mathbf{u}}_g \cdot \nabla_{\|}\overline{\Theta'^2}, \tag{11}$$

where $\mathbf{u}_g$ is the geostrophic velocity. This estimate of variance advection neglects mesoscale eddy advection and ageostrophic contributions, which are difficult to estimate from Argo data; Ekman advection of variance is neglected, as our analysis focuses on the variance response below the mixed layer.

To obtain the geostrophic velocities, $\mathbf{u}_g$, the baroclinic velocity shear was calculated using the thermal-wind balance; for the x direction, $\partial u_g/\partial z = N^2 S_y/f$, where f is the Coriolis frequency and S_y, the slope of the density surfaces, approximated by neutral surfaces. Neutral slopes were estimated from the planar fit of the depth of neutral surfaces versus horizontal distance. Absolute geostrophic velocities, $\mathbf{u}_g$, were obtained by adding a reference-depth velocity, estimated from Argo float drift at the parking depth of 1,000 m (Ollitrault et al., 2026). The variance gradients along neutral surfaces, $\nabla_{\|}\overline{\Theta'^2}$, were also evaluated from a planar fit of Θ'^2 versus horizontal distance.

Finally, the isopycnal variance production, $P_{\|,\Theta}$, was calculated as a residual of dissipation, diapycnal production and advection of tracer variance from the temperature variance budget (Equation 8),

$$P_{\|,\Theta} = \chi_\Theta - P_{\perp,\Theta} + \frac{D\overline{\Theta'^2}}{Dt}, \tag{12}$$

with the implied isopycnal diffusivities diagnosed from Equation 7,

$$K_{\|,\Theta} = \frac{\chi_\Theta - P_{\perp,\Theta} + \frac{D\overline{\Theta'^2}}{Dt}}{2\left(\nabla_{\|}\overline{\Theta}\right)^2}. \tag{13}$$

Equivalent diagnostics for absolute salinity are reported in Supporting Information S1.

4. Analyses of Tracer Variance From Argo Data

The temperature variance budget is presented along different density surfaces within the subtropical thermocline, with γ^n ranging from 26.75 to 27.65 kg m^{-3}, spanning depths of ∼200 m to ∼1,000 m.

4.1. Variance Cascade

The lifecycle of temperature variance in the North Atlantic is illustrated by mapping where variance accumulates and is transported, and eventually dissipated (Figures 1a–1c). The time-mean distribution of thermal variance, $\overline{\Theta'^2}$, is heterogeneous over the basin (Figure 1a). On lighter isopycnals $\left(\gamma^n = 26.75\ \text{kg m}^{-3}\right)$, large values of thermal variance, $\overline{\Theta'^2} > 10^{-1}\ \text{K}^2$, accumulate near subtropical gyre boundaries, where temperature contours are closely spaced. Maxima in thermal variance occur toward the western side and near the northern outcrop regions. In contrast, small variance values, $\overline{\Theta'^2} < 10^{-2}\ \text{K}^2$, occur in the centre of the subtropical gyre. Along denser isopycnals $\left(\gamma^n > 27.2\ \text{kg m}^{-3}\right)$, thermal variance generally decreases across most of the domain, although elevated values persist along the northern flank of the subtropical gyre and extend eastward into subpolar latitudes.

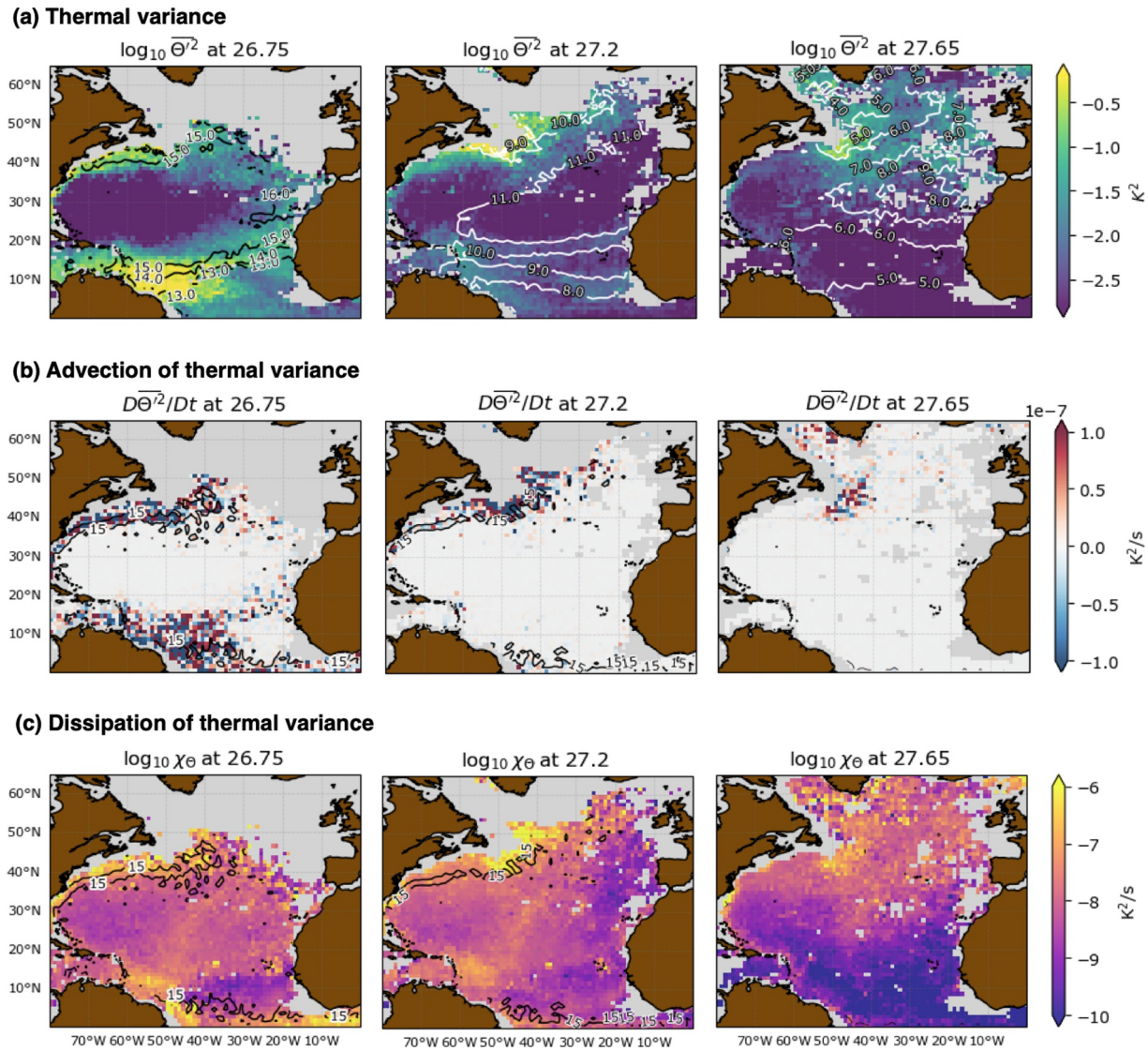

Figure 1. Thermal variance distribution and cascade. Time-mean (2006–2025) maps of (a) variance, $\overline{\Theta'^2}$, (b) advection of variance, $D\overline{\Theta'^2}/Dt$, and (c) dissipation of variance, χ_Θ, on the γ_n =26.75 (left), 27.2 (centre) and 27.65 kg m^{-3} (right) isopycnals. Contours in (a) indicate conservative temperature, Θ, every 1°C, while in panels (b, c) they indicate the isotach of 15 cm s^{-1} geostrophic velocity on the correspondent isopycnal.

The advection of thermal variance, $D\overline{\Theta'^2}/Dt$, reveals characteristic patterns consistent with the gyre-scale circulations (Figure 1b). High absolute values of variance advection, $D\overline{\Theta'^2}/Dt > 10^{-7}$ K^2 s^{-1}, occur along the flanks of the gyres on lighter isopycnals $\left(\gamma^n = 26.75 \text{ kg m}^{-3}\right)$ and extend northward on the denser isopycnal $\left(\gamma^n = 27.2 \text{ kg m}^{-3}\right)$. Another band of high magnitudes of variance advection is present along the equatorial zone. Enhanced $D\overline{\Theta'^2}/Dt$ values are connected to geostrophic streamlines following the path of the Gulf Stream and North Atlantic Current. On denser isopycnals $\left(\gamma^n = 27.65 \text{ kg m}^{-3}\right)$, the highest values of $D\overline{\Theta'^2}/Dt$ are confined to the North Atlantic Current and the Labrador Sea. Localized areas of elevated variance advection are noticeable across the subpolar gyre. Patches of positive and negative variance divergence alternate at the grid-box scale, probably due to the combination of time-mean flow patterns with variance gradients.

Diagnostics of the time-mean dissipation of thermal variance, χ_Θ (Figure 1c), are broadly aligned with the distributions of variance and variance transport, exhibiting the highest rates of dissipation, $\chi_\Theta > 10^{-7}$ K^2 s^{-1}, in the gyre's western boundaries, and in near-equatorial regions on light isopycnals (26.75–27.2 kg m^{-3}). There is

enhanced χ_Θ linked to the mid-Atlantic ridge. On denser isopycnals ($\gamma^n = 27.65\,\mathrm{kg\,m^{-3}}$), a north-south contrast is noticeable, with the lowest rates of dissipation in tropical regions, and larger rates toward the northern areas, in line with $\overline{\Theta'^2}$ patterns. On these isopycnals, dissipation rates are high along the North Atlantic Current into the eastern subpolar gyre.

4.2. Variance Budget

The thermal variance budget is now addressed for different density surfaces (Equation 8):

$$\underbrace{P_{\parallel,\Theta}}_{\substack{\text{mesoscale}\\ \text{isopycnal}\\ \text{production}}} + \underbrace{P_{\perp,\Theta}}_{\substack{\text{microscale}\\ \text{diapycnal}\\ \text{production}}} = \underbrace{\chi_\Theta}_{\substack{\text{molecular}\\ \text{dissipation}}} + \underbrace{\frac{D\overline{\Theta'^2}}{Dt}}_{\substack{\text{advection}}}, \tag{14}$$

On the lightest density surface ($\gamma^n = 26.75\,\mathrm{kg\,m^{-3}}$), the diapycnal variance production, $P_{\perp,\Theta}$, is highest ($> 10^{-8}$ $\mathrm{K^2\ s^{-1}}$) along the gyre boundaries, over the mid-Atlantic ridge and in a band along the equator (Figure 2a). Elsewhere $P_{\perp,\Theta}$ is relatively homogeneous. At intermediate densities ($\gamma^n = 27.2\,\mathrm{kg\,m^{-3}}$), there is a similar pattern of high $P_{\perp,\Theta}$, but extending further along the North Atlantic Current into the subpolar gyre. On the densest surface ($\gamma^n = 27.65\,\mathrm{kg\,m^{-3}}$), $P_{\perp,\Theta}$ decreases over the tropics and subtropics south of 30°N, and attains rates as low as $P_{\perp,\Theta} < 10^{-10}$ $\mathrm{K^2\ s^{-1}}$, and north of 30°N reaches moderate rates of $<10^{-9}$ $\mathrm{K^2\ s^{-1}}$.

The absolute values of the variance advection (Figure 2b), $|D\overline{\Theta'^2}/Dt|$, are comparable to those of $P_{\perp,\Theta}$, but reveal an imprint of the gyre circulation. On isopycnals $<27.2\,\mathrm{kg\,m^{-3}}$, elevated values of $|D\overline{\Theta'^2}/Dt|$ ($>10^{-8}$ $\mathrm{K^2\ s^{-1}}$), occur in regions of strong flow at the gyre's boundaries, frequently exceeding $P_{\perp,\Theta}$. The lowest rates of $|D\overline{\Theta'^2}/Dt|$ ($<10^{-9}$ $\mathrm{K^2\ s^{-1}}$), occur in the centre of the gyre across all density layers. On denser surfaces ($\gamma^n = 27.65\,\mathrm{kg\,m^{-3}}$), high $|D\overline{\Theta'^2}/Dt|$ ($>10^{-8}$ $\mathrm{K^2\ s^{-1}}$), occur in the subpolar region, particularly along the North Atlantic Current, but it decreases to $|D\overline{\Theta'^2}/Dt| < 10^{-10}$ $\mathrm{K^2\ s^{-1}}$ on the southern flank of the subtropical gyre, south of 26°N.

The largest isopycnal production rates, $P_{\parallel,\Theta} > 10^{-7}$ $\mathrm{K^2\ s^{-1}}$, occur in regions where variance and variance advection are high, especially along the northern and southwestern flanks of the subtropical gyre on isopycnals lighter than $27.2\,\mathrm{kg\,m^{-3}}$ (Figure 2c). Isopycnal production is moderately enhanced over the mid-Atlantic ridge, $P_{\parallel,\Theta} > 10^{-9}$ $\mathrm{K^2\ s^{-1}}$, coinciding with elevated $P_{\perp,\Theta}$. At the densest surface ($27.65\,\mathrm{kg\,m^{-3}}$), high rates of isopycnal production, $P_{\parallel,\Theta} > 10^{-8}$ $\mathrm{K^2\ s^{-1}}$, occur in the northernmost part of the Gulf Stream, the North Atlantic Current and most of the subpolar gyre, concurrent to substantial advection.

There are implied negative values of isopycnal production that may be due to errors in closing our budget (since the isopycnal transfer is diagnosed as a residual), or could point to up-gradient isopycnal mesoscale eddy fluxes. On light isopycnals, these negative values cluster around areas of strong isopycnal stirring and variance advection, suggesting a plausible physical signature with non-local balances and up-gradient fluxes. On denser neutral surfaces, negative signals are more scattered, potentially signaling methodological uncertainties.

5. Mixing Regimes

The lifecycle of tracer variance involves different balances in the variance budget, and so defines distinct mixing regimes. These regimes are highlighted by the relative contributions of diapycnal production, $P_{\perp,\Theta}$ (indicative of diapycnal stirring), and transport of variance, $D\overline{\Theta'^2}/Dt$, with respect to dissipation of temperature variance, χ_Θ, as plotted on different density surfaces (Figures 3a and 3d).

The contribution of diapycnal stirring is relatively small in areas of enhanced thermal variance, indicating that isopycnal stirring dominates variance dissipation (Figure 3a). Isopycnal stirring is dominant along gyre boundaries for light isopycnals ($\gamma^n < 27.2\,\mathrm{kg\,m^{-3}}$), and in subpolar regions for denser isopycnals ($\gamma^n = 27.65\,\mathrm{kg\,m^{-3}}$). In contrast, the centre of the subtropical gyre, characterized by weak thermal variance, is dominated by diapycnal

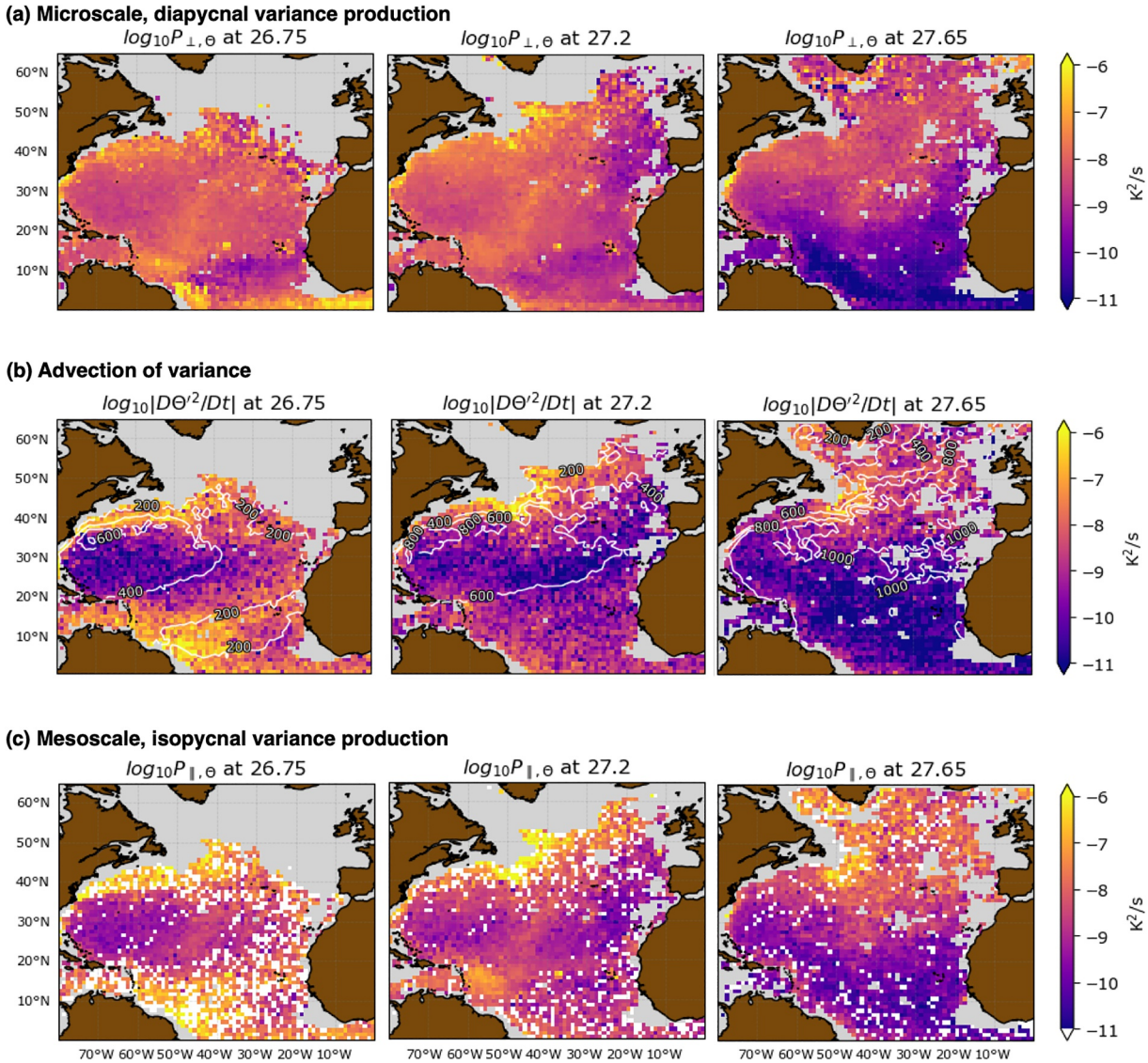

Figure 2. Thermal variance budget. Time-mean maps (for years 2006–2024) of (a) diapycnal production of variance, $P_{\perp,\Theta}$, (b) absolute values of variance advection, $|D\overline{\Theta'^2}/Dt|$, and (c) isopycnal variance production, $P_{\parallel,\Theta}$ on the γ_n =26.75 (left), 27.2 (centre) and 27.65 (right) kg m^{-3} isopycnals. White areas in panel (c) indicate negative $P_{\parallel,\Theta}$ values due to larger, negative advection of variance $|D\overline{\Theta'^2}/Dt|$, compared to the residual variance production $(\chi_\Theta - P_{\perp,\Theta})$. Contours in panel (b) indicate the depth of the given isopycnal every 200 m.

stirring. Although the general spatial pattern is repeated for different density surfaces, the overall relative importance of diapycnal stirring decreases with density.

Hence, two distinct mixing regimes have been identified thus far: isopycnal stirring dominates along gyre boundaries and in the subpolar gyre, and diapycnal stirring prevails over the core of the subtropical gyre.

5.1. Controls on Mixing Regimes

Patterns in variance production rates stem from the interplay between patterns in diapycnal and isopycnal diffusivities and in property gradients (Equation 7). Therefore, controls on the mixing regimes may be assessed by comparing the relative importance of spatial variations in turbulent diffusivities versus property gradients. To perform this assessment, the ratio between diapycnal production and total dissipation rates, $P_{\perp,\Theta}/\chi_\Theta$, is quantified, while keeping either the turbulent diffusivities or the tracer gradients constant. Thus, $P_{\perp,\Theta}/\chi_\Theta$ is evaluated using either spatial-mean diffusivities (Figure 3b)

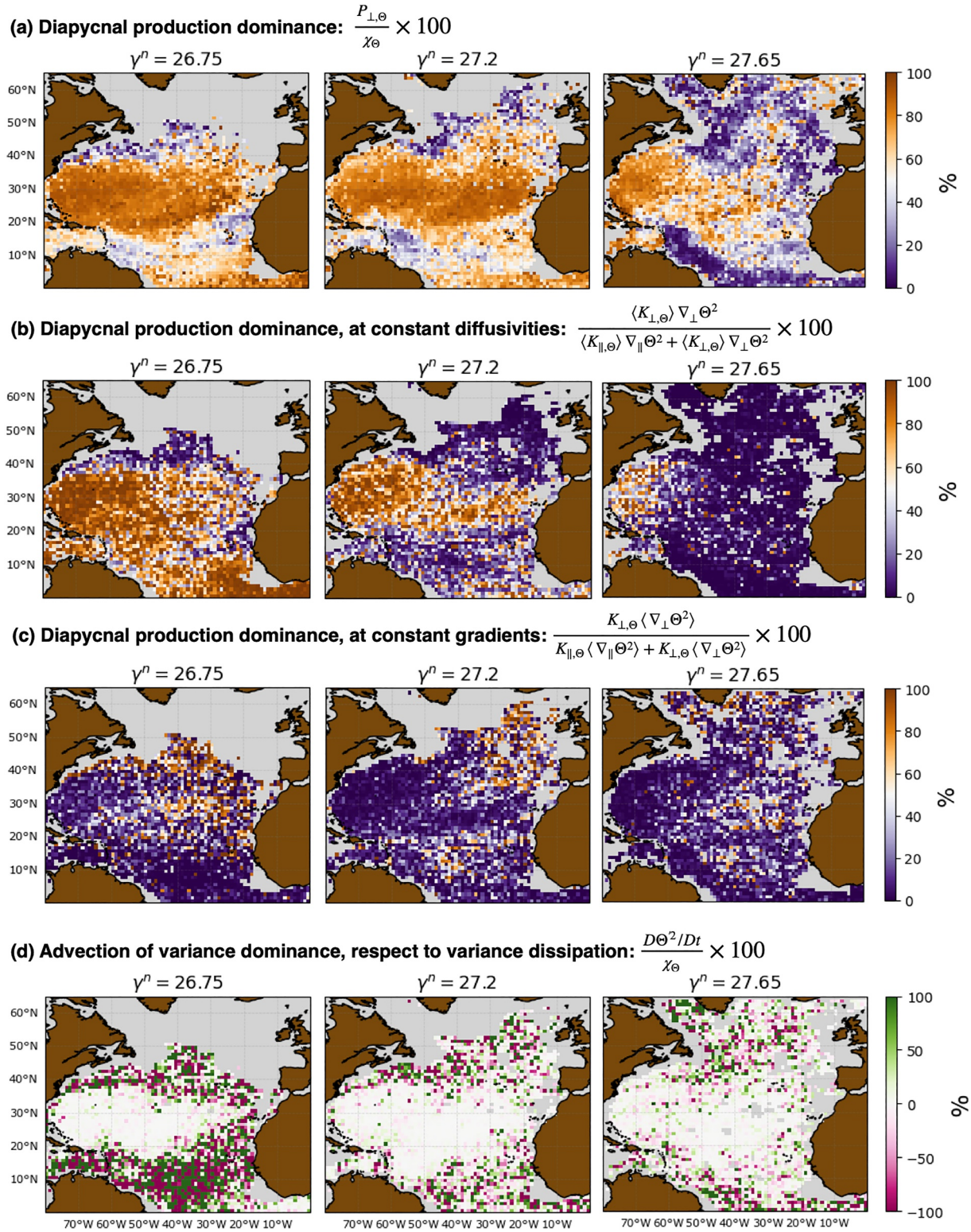

Figure 3. Mixing regimes and vertical structure. Time-mean (2006–2024) maps of the ratio of (a) diapycnal production of thermal variance over dissipation, $P_{\perp,\Theta}/\chi_\Theta$, (b) diapycnal production over dissipation at spatially constant diffusivities, $\langle K_\perp \rangle$ and $\langle K_{\parallel,\Theta} \rangle$, (c) diapycnal production over dissipation at spatially constant squared gradients, $\langle \nabla_\perp \Theta^2 \rangle$ and $\langle \nabla_\parallel \Theta^2 \rangle$, and (d) ratio of advection of thermal variance to dissipation, $\left(D\Theta'^2/Dt\right)/\chi_\Theta$.

$$r_1 = \frac{\langle K_{\perp,\Theta} \rangle \left(\nabla_\perp \overline{\Theta}\right)^2}{\langle K_{\parallel,\Theta} \rangle \left(\nabla_\parallel \overline{\Theta}\right)^2 + \langle K_{\perp,\Theta} \rangle \left(\nabla_\perp \overline{\Theta}\right)^2}, \tag{15}$$

or spatial-mean tracer gradients (Figure 3c):

$$r_2 = \frac{K_{\perp,\Theta} \langle \left(\nabla_\perp \overline{\Theta}\right)^2 \rangle}{K_{\parallel,\Theta} \langle \left(\nabla_\parallel \overline{\Theta}\right)^2 \rangle + K_{\perp,\Theta} \langle \left(\nabla_\perp \overline{\Theta}\right)^2 \rangle}, \tag{16}$$

where the brackets $\langle\ \rangle$ represent a spatial average on a density surface over the whole North Atlantic.

The spatial distribution of mixing regimes (Figure 3a) is more closely reproduced in the scenario of uniform diffusivities (Figure 3b), indicating that variations in the diffusivities themselves play a secondary role in setting these regimes. Instead, tracer gradients primarily govern the spatial configuration of mixing regimes across the North Atlantic. This interpretation is consistent with the general lack of similarity between Figures 3a and 3c.

5.2. Relative Importance of Variance Advection

The ratio of the advection of thermal variance to dissipation, expressed as $\left(D\overline{\Theta'^2}/Dt\right)/\chi_\Theta$ (Figure 3d), reveals that in dynamical regions where thermal variance is high, the variance budget is controlled by advective processes rather than by local dissipation, $|D\overline{\Theta'^2}/Dt| > \chi_\Theta$. Since the advection term can take either sign, this ratio may be positive or negative. A negative ratio indicates that advection leads to an increase of thermal variance, transporting variance into the region, while a positive ratio indicates that advection decreases thermal variance. In both cases, the implication is that variance is not being produced and dissipated locally. Instead, the evolution of the variance is affected by the transport of variance from other parts of the domain.

We assessed how the relative importance of variance advection depends on the spatial scale of analysis by binning the Argo data in coarser 3-degree boxes. At those larger scales, variance transport appears relatively unimportant, and instead there is a local balance between tracer variance sources and sinks (Figures S5–S7 in Supporting Information S1). The relative importance of variance advection increases with decreasing scale: advection by the mean flow, and potentially mesoscale and submesoscale flows, may become dominant at progressively smaller scales close to the Rossby radius.

5.3. Connection to Water-Mass Distributions

Given the strong connection between mixing regimes and temperature gradients, the regimes can potentially be understood in terms of different water-masses, as represented in temperature–salinity space (Figure 4a and Figure S8 in Supporting Information S1). Elevated rates of thermal variance dissipation, $\chi_\Theta > 5 \times 10^{-7}\ \mathrm{K^2\ s^{-1}}$, follow major water-mass boundaries (Speer & Forget, 2013):

1. High rates of dissipation, χ_Θ, occur on density surfaces lighter than $27.0\ \mathrm{kg\ m^{-3}}$, located between the two thermoclines in the region, that is, the cooler-fresher thermocline associated with South Atlantic Central Water (SACW) present at the domain's southern edge, and the warmer-saltier thermocline associated with North Atlantic Central Water (NACW).
2. Elevated dissipation rates also occur on denser surfaces, $> 27.0\ \mathrm{kg\ m^{-3}}$, connected to the interaction between Labrador Sea Water (LSW) and Mediterranean Water (MW), as well as to fresh and cold Arctic Waters (< 5°C and $< 34\ \mathrm{g\ kg^{-1}}$).

These areas of elevated dissipation of thermal variance (Figure 4a) often correspond to mixing regimes with a dominance of isopycnal production, as defined by low values of $P_\perp/\chi_\Theta$ (Figure 4b, purple regions).

Hence, strongest mixing rates occur where large-volume water masses meet, generating thermohaline gradients, which are then stirred primarily along isopycnals.

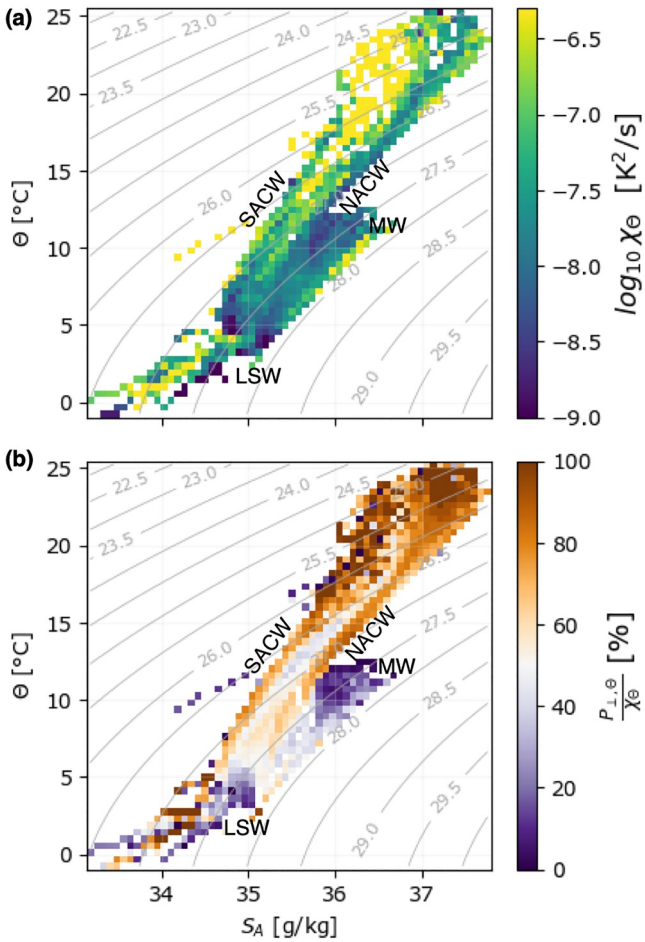

Figure 4. Connections between mixing regimes and water-mass distributions. Volume-weighted temperature-salinity diagrams: (a) dissipation of thermal variance, χ_Θ ($K^2 s^{-1}$) and (b) the ratio of diapycnal thermal variance production to thermal variance dissipation, $\frac{P_{\Theta,\perp}}{\chi_\Theta}$. Main water masses are labeled (lightest to densest): South Atlantic Central Water, SACW; North Atlantic Central Water, NACW; Mediterranean Water, MW; and Labrador Sea Water, LSW.

6. Conclusions

Mesoscale and microscale stirring play a crucial role in determining temperature-salinity distributions in the ocean interior, acting to reduce property contrasts originally created by surface forcing in the mixed layer and subsequent ventilation. Microscale stirring is isotropic and mainly alters properties diapycnally, while mesoscale stirring acts preferentially along density surfaces. A tracer variance budget has previously been used to separate the contributions of microscale and mesoscale turbulence using microstructure observations (Ferrari & Polzin, 2005; Fernández Castro et al., 2024; Naveira Garabato et al., 2016). However, these analyses assume a local balance between sources and sinks of tracer variance. Instead ocean circulation models reveal that transport of variance is an important contribution (Rhines & Holland, 1979), explaining the direction of mesoscale eddy potential vorticity fluxes (Wilson & Williams, 2006) and varying with ocean storm tracks (Williams et al., 2007).

Here, we explored the variance budget for temperature including an estimate of variance transport (and salinity, see Supporting Information S1) over the North Atlantic using two decades of Argo data (Broullón et al., 2026b). The transport of tracer variance is estimated from the time-mean geostrophic flow and ignores any Ekman contributions as our diagnostics are below the mixed layer. We are unable to evaluate the mesoscale eddy advection of variance due to the constraints of the data, although eddy-resolving model studies find that term is important for mesoscale eddy circulations (Wilson & Williams, 2004).

Our analyses reveal three distinct mixing regimes over the North Atlantic. First, in the thermocline of the central subtropical gyre, a local balance holds between diapycnal production of variance by microscale turbulence and dissipation of variance by molecular processes. Second, in denser isopycnals spanning intermediate waters, variance dissipation is primarily balanced by isopycnal eddy stirring. The isopycnal-stirring mixing regime is restricted mainly to the deep thermocline at subtropical latitudes, but reaches the upper ocean in subpolar latitudes. Third, a new mixing regime is identified for dynamic gyre boundary regions, occurring on the northern and southern flanks of the subtropical gyre. In this regime of strong flows, variance production is dominated by isopycnal stirring and variance advection leads to a local mismatch between variance sources and sinks.

The first two mixing regimes, with diapycnal stirring dominating in the subtropical thermocline and isopycnal stirring prevalence in intermediate waters, are consistent with regional microstructure studies (Fernández Castro et al., 2024; Ferrari & Polzin, 2005) and global-scale climatological assessments of mixing processes (Fernández Castro et al., 2026; Sévellec et al., 2025). The primary control of these two mixing regimes is the distribution of property gradients with regions of high variance dissipation corresponding to water-mass boundaries and a prevalence of isopycnal stirring.

For the new dynamically active regime, including strong background flows and large isopycnal property contrasts, the lifecycle of tracer variance unfolds over a relatively extensive domain, where tracer variance production and dissipation are separated by hundreds of kilometres. For frontal jets along gyre boundaries, such as the Gulf Stream and North Atlantic Current, there is a disconnection between the processes producing and dissipating tracer variance. Any misrepresentation of the variance lifecycle here is expected to affect along-stream modification of water masses by mixing, altering properties of water masses transferred across the gyre-bounding fronts. For example, the Gulf Stream provides an accompanying nutrient stream, supplying nutrients to subpolar latitudes (Pelegrí et al., 1996) as well as sub-surface waters depleted in anthropogenic carbon, which together

affect subpolar carbon uptake (Williams et al., 2026). The downstream changes in transport-weighted tracers carried along the nutrient stream are affected by the relative importance of isopycnal stirring or diapycnal mixing (Whitt, 2019; Williams et al., 2011).

Our diagnostics of the lifecycle of tracer variance revealing different mixing regimes should carry over to the rest of the global ocean. Mesoscale stirring is expected to dominate whenever there are strong water-mass contrasts on density surfaces. A mismatch between sources and sinks of tracer variance is expected to occur in dynamically-active regions, such as western boundary currents and more zonal jets in the tropics and Southern Ocean, where the circulation is sufficiently strong to provide significant variance transport. These different mixing regimes are climatically important, since differing strengths of mesoscale and diapycnal stirring alter the distribution of anthropogenic heat in the thermocline (Li et al., 2023), and so affect how the global ocean sequesters heat.

Appendix A: Tracer Variance Equation

The tracer equation is given by

$$\frac{\partial c}{\partial t} + \mathbf{u} \cdot \nabla c = \nabla \cdot (\kappa_c \nabla c), \tag{A1}$$

where c is a generic tracer, $\mathbf{u}$ is the three-dimensional velocity and κ_c is molecular diffusivity; here a Boussinesq approximation is made where density changes are neglected (Davis, 1994). A Reynolds decomposition is applied to (Equation A1) with variables separated into a time mean (denoted by an overbar), representing an average over many eddy lifecycles, and a temporal eddy deviation (denoted by a prime), such that $c = \overline{c} + c'$ and $\mathbf{u} = \overline{\mathbf{u}} + \mathbf{u}'$, so that the time-mean tracer balance is

$$\overline{\mathbf{u}}.\nabla\overline{c} + \overline{\mathbf{u}'.\nabla c'} = \nabla.(\kappa_c \nabla\overline{c}). \tag{A2}$$

The evolution of the tracer perturbation, from (Equation A1) minus (Equation A2), is given by

$$\frac{\partial c'}{\partial t} + \mathbf{u} \cdot \nabla c' + \mathbf{u}' \cdot \nabla\overline{c} - \overline{\mathbf{u}' \cdot \nabla c'} = \nabla \cdot (\kappa_c \nabla c'). \tag{A3}$$

The tracer variance equation is obtained by multiplying (Equation A3) by $2c'$,

$$\frac{\partial c'^2}{\partial t} + \mathbf{u} \cdot \nabla c'^2 + 2c'\mathbf{u}' \cdot \nabla\overline{c} - 2c'\overline{\mathbf{u}' \cdot \nabla c'} = 2c'\nabla \cdot (\kappa_c \nabla c'), \tag{A4}$$

and then time averaging, such that

$$\frac{\partial\overline{c'^2}}{\partial t} + \overline{\mathbf{u} \cdot \nabla c'^2} + 2\overline{\mathbf{u}'c'} \cdot \nabla\overline{c} = 2\overline{c'\nabla \cdot (\kappa_c \nabla c')}, \tag{A5}$$

where the term $\overline{2c'}\,\overline{\mathbf{u}'.\nabla c'}$ vanishes through the time average. The product rule is used to express the right-hand side of (Equation A5), so that

$$\overline{c'\nabla.(\kappa_c \nabla c')} = \nabla.\overline{(c'\kappa_c \nabla c')} - \kappa_c\overline{(\nabla c')^2}. \tag{A6}$$

Hence, by combining (Equation A5) and (Equation A6), the tracer variance equation is written in advective form as

$$\frac{\partial\overline{c'^2}}{\partial t} + \overline{\mathbf{u} \cdot \nabla c'^2} + \nabla \cdot \left(-\kappa_c \nabla\overline{c'^2}\right) + 2\overline{\mathbf{u}'c'} \cdot \nabla\overline{c} = -2\kappa_c\overline{(\nabla c')^2}, \tag{A7}$$

or equivalently in divergence form (Davis, 1994; Ferrari & Polzin, 2005; Garrett, 2001) as

$$\underbrace{\frac{\partial \overline{c'^2}}{\partial t}}_{\substack{\text{tendency}\\ \text{of variance}}} + \underbrace{\nabla \cdot \left(\overline{\mathbf{u}c'^2} - \kappa_c \nabla \overline{c'^2}\right)}_{\substack{\text{divergence of}\\ \text{variance transport}}} + \underbrace{2\overline{\mathbf{u}'c'} \cdot \nabla \overline{c}}_{\substack{\text{eddy production}\\ \text{of variance}}} = \underbrace{-2\kappa_c \overline{(\nabla c')^2}}_{\substack{\text{dissipation}\\ \text{of variance}}}, \tag{A8}$$

where the advective variance transport $\overline{\mathbf{u}\,c'^2}$ is made up of contributions from the time-mean flow and by mesoscale eddies,

$$\overline{\mathbf{u}\,c'^2} = \overline{\mathbf{u}}\,\overline{c'^2} + \overline{\mathbf{u}'c'^2}. \tag{A9}$$

Conflict of Interest

The authors declare no conflicts of interest relevant to this study.

Availability Statement

Argo data were collected and made freely available by the International Argo Program and the national programs that contribute to it (https://argo.ucsd.edu, https://www.ocean-ops.org). The Argo Program is part of the Global Ocean Observing System. *argopy* software was used to download the data (Maze & Balem, 2020). Velocities from Argo parking depths at 1,000 m have been obtained from Ollitrault et al. (2026). The shear-strain parameterisation is implemented from the *mixsea* package for Python (Voet et al., 2023). Code used for the mixing diagnostics and the creation of the figures is available in Broullón et al. (2026a).

Acknowledgments
This work was supported by an European Research Council-Consolidator Grant 101169952 (REMIX-TUNE), an Advanced Research and Invention Agency-Forecasting Tipping Points Grant SCOP-PR01-P021 (POLEMIX), and a UK Natural Environment Research Council Grant NE/W009501/1 (C-Streams). We thank Stephen Griffies and an anonymous referee for constructive comments that strengthened the study.

References

Argo. (2025). *Argo float data and metadata from Global Data Assembly Centre (Argo GDAC)* (Technical Report). SEANOE.

Broullón, E., Fernández Castro, B., Naveira Garabato, A., Clement, L., & Williams, R. (2026a). Python code for the paper "The lifecycle of tracer variance in the North Atlantic". *Zenodo*. https://doi.org/10.5281/zenodo.19679248

Broullón, E., Fernández Castro, B., Naveira Garabato, A. C., Clément, L., Oltmanns, M., & Williams, R. G. (2026b). Isopycnal stirring and diapycnal mixing in the eastern North Atlantic inferred from Argo observations. *Journal of Physical Oceanography*, *56*(3), 627–641. https://doi.org/10.1175/jpo-d-25-0090.1

Cherian, D., Guo, Y., & Bryan, F. (2024). Assessing modeled mesoscale stirring using microscale observations. *Journal of Physical Oceanography*, *54*(5), 1183–1194. https://doi.org/10.1175/jpo-d-23-0135.1

Davis, R. E. (1994). Diapycnal mixing in the ocean: The Osborn–Cox model. *Journal of Physical Oceanography*, *24*(12), 2560–2576. https://doi.org/10.1175/1520-0485(1994)024<2560:dmitot>2.0.co;2

Döös, K., Nilsson, J., Nycander, J., Brodeau, L., & Ballarotta, M. (2012). The World Ocean thermohaline circulation. *Journal of Physical Oceanography*, *42*(9), 1445–1460. https://doi.org/10.1175/JPO-D-11-0163.1

Fernández Castro, B., Fernández Román, D., Ferron, B., Fontela, M., Lherminier, P., Naveira Garabato, A., et al. (2024). Isopycnal Eddy stirring dominates thermohaline mixing in the upper subpolar North Atlantic. *Journal of Geophysical Research: Oceans*, *129*(9), e2023JC020817. https://doi.org/10.1029/2023JC020817

Fernández Castro, B., Groeskamp, S., Broullón, E., Clément, L., Evans, D. G., Garabato, A. C. N., & Williams, R. G. (2026). Global observational estimates of thermohaline transformations by interior ocean mixing. *Journal of Physical Oceanography*, *56*(5), 1051–1076. https://doi.org/10.1175/JPO-D-25-0265.1

Ferrari, R., & Polzin, K. L. (2005). Finescale structure of the T-S relation in the eastern North Atlantic. *Journal of Physical Oceanography*, *35*(8), 1437–1454. https://doi.org/10.1175/JPO2763.1

Garrett, C. (1983). On the initial streakness of a dispersing tracer in two- and three-dimensional turbulence. *Dynamics of Atmospheres and Oceans*, *7*(4), 265–277. https://doi.org/10.1016/0377-0265(83)90008-8

Garrett, C. (2001). Stirring and mixing: What are the rate-controlling processes? From stirring to mixing in a stratified ocean. In *Proceedings' AhaHuliko'a winter workshop* (pp. 1–8).

Groeskamp, S., Griffies, S. M., Iudicone, D., Marsh, R., Nurser, A. G., & Zika, J. D. (2019). The water mass transformation framework for ocean physics and biogeochemistry. *Annual Review of Marine Science*, *11*(1), 271–305. https://doi.org/10.1146/annurev-marine-010318-095421

Hieronymus, M., Nilsson, J., & Nycander, J. (2014). Water mass transformation in salinity-temperature space. *Journal of Physical Oceanography*, *44*(9), 2547–2568. https://doi.org/10.1175/JPO-D-13-0257.1

Holland, W. R., & Rhines, P. B. (1980). An example of eddy-induced ocean circulation. *Journal of Physical Oceanography*, *10*(7), 1010–1031. https://doi.org/10.1175/1520-0485(1980)010<1010:aeoeio>2.0.co;2

Jackett, D. R., & McDougall, T. J. (1997). A neutral density variable for the World's Oceans. *Journal of Physical Oceanography*, *27*(2), 237–263. https://doi.org/10.1175/1520-0485(1997)027⟨0237:ANDVFT⟩2.0.CO;2

Joyce, T. M. (1977). A note on the lateral mixing of water masses. *Journal of Physical Oceanography*, *7*(4), 626–629. https://doi.org/10.1175/1520-0485(1977)007<0626:anotlm>2.0.co;2

Kunze, E., Firing, E., Hummon, J. M., Chereskin, T. K., & Thurnherr, A. M. (2006). Global abyssal mixing inferred from lowered ADCP shear and CTD strain profiles. *Journal of Physical Oceanography*, *36*(8), 1553–1576. https://doi.org/10.1175/JPO2926.1

Ledwell, J. R., Watson, A. J., & Law, C. S. (1998). Mixing of a tracer in the pycnocline. *Journal of Geophysical Research*, *103*(C10), 21499–21529. https://doi.org/10.1029/98JC01738

Li, Z., England, M. H., & Groeskamp, S. (2023). Recent acceleration in global ocean heat accumulation by mode and intermediate waters. *Nature Communications*, *14*(1), 6888. https://doi.org/10.1038/s41467-023-42468-z

MacGilchrist, G. A., Johnson, H. L., Marshall, D. P., Lique, C., Thomas, M., Jackson, L. C., & Wood, R. A. (2020). Locations and mechanisms of ocean ventilation in the high-latitude North Atlantic in an eddy-permitting ocean model. *Journal of Climate*, *33*(23), 10113–10131. https://doi.org/10.1175/JCLI-D-20-0191.1

Marshall, J. C. (1984). Eddy-mean-flow interaction in a barotropic ocean model. *Quarterly Journal of the Royal Meteorological Society*, *110*(465), 573–590. https://doi.org/10.1256/smsqj.46501

Marshall, J. C., Williams, R. G., & Nurser, A. G. (1993). Inferring the subduction rate and period over the North Atlantic. *Journal of Physical Oceanography*, *23*(7), 1315–1329. https://doi.org/10.1175/1520-0485(1993)023<1315:itsrap>2.0.co;2

Maze, G., & Balem, K. (2020). Argopy: A python library for argo ocean data analysis. *Journal of Open Source Software*, *5*(52), 2425. https://doi.org/10.21105/joss.02425

Naveira Garabato, A. C., Ferrari, R., & Polzin, K. (2011). Eddy stirring in the Southern Ocean. *Journal of Geophysical Research*, *116*(C9), C09019. https://doi.org/10.1029/2010jc006818

Naveira Garabato, A. C., Polzin, K. L., Ferrari, R., Zika, J. D., & Forryan, A. (2016). A microscale view of mixing and overturning across the Antarctic Circumpolar Current. *Journal of Physical Oceanography*, *46*(1), 233–254. https://doi.org/10.1175/JPO-D-15-0025.1

Ollitrault, M., Rannou, P., Brion, E., Cabanes, C., Piron, A., Reverdin, G., et al. (2026). *ANDRO: An Argo-based deep displacement dataset*. SEANOE. https://doi.org/10.17882/47077

Osborn, T. R., & Cox, C. S. (1972). Oceanic fine structure. *Geophysical Fluid Dynamics*, *3*(4), 321–345. https://doi.org/10.1080/03091927208236085

Pelegrí, J. L., Csanady, G. T., & Martins, A. (1996). The North Atlantic nutrient stream. *Journal of Oceanography*, *52*(3), 275–299. https://doi.org/10.1007/BF02235924

Rhines, P. B., & Holland, W. R. (1979). A theoretical discussion of eddy-driven mean flows. *Dynamics of Atmospheres and Oceans*, *3*(2–4), 289–325. https://doi.org/10.1016/0377-0265(79)90015-0

Sévellec, F., Kolodziejczyk, N., & Portela, E. (2025). Turbulent isopycnal mixing dominates thermohaline transformations of intermediate ocean waters. *Nature Communications*, *16*(1), 9838. https://doi.org/10.1038/s41467-025-64806-z

Smith, K. S., & Ferrari, R. (2009). The production and dissipation of compensated thermohaline variance by mesoscale stirring. *Journal of Physical Oceanography*, *39*(10), 2477–2501. https://doi.org/10.1175/2009JPO4103.1

Speer, K., & Forget, G. (2013). Global distribution and formation of mode waters. In *International geophysics* (Vol. 103, pp. 211–226). Elsevier. https://doi.org/10.1016/b978-0-12-391851-2.00009-x

Sundermeyer, M. A., & Price, J. F. (1998). Lateral mixing and the north Atlantic tracer release experiment: Observations and numerical simulations of Lagrangian particles and a passive tracer. *Journal of Geophysical Research*, *103*(C10), 21481–21497. https://doi.org/10.1029/98JC01999

Voet, G., Drake, H., & Cusack, J. (2023). *Modscripps/mixsea: V0.1.2*. Zenodo. https://doi.org/10.5281/zenodo.10636077

Whalen, C. B., Talley, L. D., & MacKinnon, J. A. (2012). Spatial and temporal variability of global ocean mixing inferred from Argo profiles. *Geophysical Research Letters*, *39*(17). https://doi.org/10.1029/2012GL053196

Whitt, D. B. (2019). On the role of the Gulf stream in the changing Atlantic nutrient circulation during the 21st century. In *Kuroshio current: Physical, biogeochemical, and ecosystem dynamics* (pp. 51–82).

Williams, R. G., Brown, P. J., Takano, Y., Forget, G., Jones, D., Katavouta, A., et al. (2026). The biogeochemical transport by the Gulf Stream. *Communications Earth & Environment*, *7*(1), 149. https://doi.org/10.1038/s43247-025-03118-y

Williams, R. G., McDonagh, E., Roussenov, V. M., Torres-Valdes, S., King, B., Sanders, R., & Hansell, D. A. (2011). Nutrient streams in the North Atlantic: Advective pathways of inorganic and dissolved organic nutrients. *Global Biogeochemical Cycles*, *25*(4). https://doi.org/10.1029/2010GB003853

Williams, R. G., Wilson, C., & Hughes, C. W. (2007). Ocean and atmosphere storm tracks: The role of eddy vorticity forcing. *Journal of Physical Oceanography*, *37*(9), 2267–2289. https://doi.org/10.1175/jpo3120.1

Wilson, C., & Williams, R. G. (2004). Why are eddy fluxes of potential vorticity difficult to parameterize? *Journal of Physical Oceanography*, *34*(1), 142–155. https://doi.org/10.1175/1520-0485(2004)034<0142:waefop>2.0.co;2

Wilson, C., & Williams, R. G. (2006). When are eddy tracer fluxes directed downgradient? *Journal of Physical Oceanography*, *36*(2), 189–201. https://doi.org/10.1175/jpo2841.1

Wong, A. P., Wijffels, S. E., Riser, S. C., Pouliquen, S., Hosoda, S., Roemmich, D., et al. (2020). Argo data 1999–2019: Two million temperature-salinity profiles and subsurface velocity observations from a global array of profiling floats. *Frontiers in Marine Science*, *7*, 700. https://doi.org/10.3389/fmars.2020.00700

Zika, J. D., England, M. H., & Sijp, W. P. (2012). The ocean circulation in thermohaline coordinates. *Journal of Physical Oceanography*, *42*(5), 708–724. https://doi.org/10.1175/JPO-D-11-0139.1